INTERNATIONAL JOURNAL OF MARITIME TECHNOLOGY
IJMT Vol.16/ Summer 2021 (123-134)
Available online at: www. ijmt.ir

Numerical Analysis of Hydrodynamic-Structural and Vibration of Pump Jet Propulsion System of AUV

Ehsan Yari

Assistance professor, Faculty of mechanical engineering, Malek- Ashtar University of Technology; ehsanyari11@gmail.com

ARTICLE INFO

Article History:
Received: 12 Aug. 2022
Accepted: 30 Nov. 2022

Keywords:
Pump Jet Propulsion
Hydrodynamic
Structure
Vibration
CFD

ABSTRACT

The aim of this paper is the numerical hydrodynamic, structure, and vibration analysis of a pump jet propulsion system that mounted the tail of the AUV. A home code based on the boundary element method coupled with XFOIL code is used to extract the initial pump jet geometry. Then computational fluid dynamics analysis of DTMB4119 benchmark propeller (for validation of numerical result) and desired pump jet propulsion system have carried out based on RANS method and realizable k-ε turbulence model. Pump jet geometry modification has been done so that in the maximum hydrodynamic efficiency, the maximum amount of rotor moment is neutralized by the stator moment. However, according to the obtained hydrodynamic results, the stator moment neutralizes 85% of the rotor moment in the best situation. The maximum accessible hydrodynamic efficiency of the designed pump jet propulsion is 83%. The structural analysis of the designed pump jet propulsion has been performed on the rotor, stator, hub, and duct. For structure and vibration analysis, the pressure distribution on the pump jet obtained from the CFD results is applied point by point. The pump jet is aluminum with a Young modulus of 70 GPa. Based on the obtained structural results, the rotor will not have a problem vibrating.

1. Introduction

The pump jet propulsion system is one of the marine propulsion systems that mainly has underwater applications but is also used with some modifications in surface patrol vessels. The advantage of the pump jet propulsion system compared with other marine propulsion systems can be expressed in high hydrodynamic performance and low noise [1]. Figure 1 shows an underwater marine vehicle with a pump jet propulsion system.

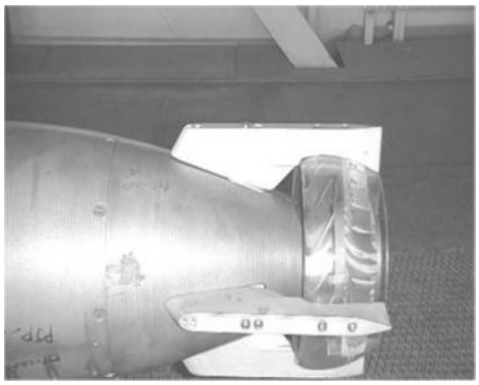

Figure.1 Pump jet propulsion of underwater marine vehicle[1]

In a simple definition, the pump jet system can be defined as a propeller assembled with an acceleration-reducing duct and fixed blades. It is a new propulsion system compared to other propulsion systems and has found many applications quickly due to its advantages. High thrust generation and low cavitation are some of the features of this system that can be a good justification for military applications. Pump jets are mostly used in AUVs, torpedoes and military marine vehicles.

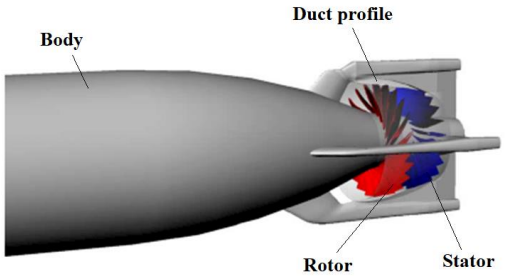

Figure.2 Pump jet propulsion system components [2]

According to Figure 2, the pump jet system consists of a rotor, stator, duct, and hub.

Some research activities are reviewed around the pump jet propulsion system in the following.

Suryanarayana et al. [1] have proposed experimental techniques for testing jet propulsion systems in wind tunnels. Zhang et al. [3] simulated three-dimensional unsteady turbulence flow in axial flow pumps based on the Navier-Stokes solver by the k-ε RNG turbulence model and the SIMPLEC algorithm. Numerical results show that the results of the transient state are more accurate than the steady state results, and the maximum error observed in the unstable state is only 4.54%. Bozorgi and Seif [4] studied the underwater body's resistance and the thrust produced by the pump jet and determined its self-propulsion point. Lu et al. [5] developed a distributed pump-jet propulsion system with special two-four pods around the SUB OFF AFF-3 model. It is shown in the calculated results that the decrease in the distance between the pods and the hull leads to an increase both in the efficiency of the pods and the thrust deduction factor due to the effect of the stern wake. In the other paper, Lu et al. [6] conducted a numerical analysis based on the unsteady Reynolds-averaged Navier-Stokes method of homogeneous multiphase using structured grids and the shear stress transport k-ω turbulence model. The numerical simulations accurately predict the propulsor efficiency changes and the cavitation inception and extension on the suction side of rotor blades. Yari and Ghassemi [7] provided an applied algorithm for analyzing propeller-shaft vibrations in underwater marine vehicles. The propeller has been analyzed using an unsteady boundary element code, and the fluctuations of the forces acting on the shaft have been extracted. The natural and forced frequency of the propeller has been determined in various vibration modes. According to obtained results, the maximum displacement is related to the propeller blade tip in a forced vibration state.

Lu et al. [8] simulated the pump jet tip clearance effects with the commercial code ANSYS CFX and structured grid. Numerical results show that the tip leakage vortex's structure and characteristics and propulsor's efficiency dropped more sharply with the tip clearance size. Lu et al. [9] studied the hydrodynamic performance of pumpjet propulsor. A numerical investigation based on the RANS method has been done. The numerical predictions of hydrodynamic performance of pumpjet propulsor were obtained at different advance ratios. Results indicate that the rotor provides the main thrust of the propulsor and the balance performance of the propulsor is generally satisfactory. Qin et al. investigated a pump jet propulsor with different sizes of tip clearances using the computational fluid dynamic method and the SST k-ω turbulen ce model [10]. Based on obtained results, the open water efficiency decreases gradually with the increase of tip clearance. In addition, the main pressure area affected by different tip clearances is mainly concentrated in the area above 0.9 spanwise of the suction side of the rotor blade. Motallebi et al. [11] performed a numerical analysis of ducted propeller and pumped jet propulsion systems using computational fluid dynamics. The RANS equations with SST k-ω turbulent model are solved in a periodic computational domain around the pump jet. Qin et al. [12] designed two types of Pump Jet Propulsion, the stator-rotor, and the rotor-stator, to investigate the difference in the hydrodynamic performance between those two types. Numerical results were extracted using an improved Delayed Detached Eddy Simulation model. Spiral precession and double-helix breakdown of hub vortex had observed for the stator-rotor PJP. Jian et al. [13] have studied the effect of the gap flow model on predicting the hydrodynamic performance of pump jet propulsor. Based on obtained results, the gap flow model reflects the circulation and pressure distribution of the rotor blade as well as the pressure differential force distribution between the blade surface and the back of the blade. Su et al. [14] have presented the unsteady simulation of the excitations from a pump-jet running in the downstream wake of a SUB OFF model and the vibroacoustic characteristics of a coupled pump jet–a shafting system under unsteady excitations.

This study aims to design and numerically analyze the pump jet system in reaction with the body. The structure of the pump jet system was investigated using Abacus software with the help of a home code to define the force field on the blades, duct, and hub. At the end of the article, the vibration analysis of the pump jet system is performed. In fact, in this paper, the process of design and numerical analysis of hydro-structural and vibration of pump jet system has been done.

2. Geometry

Figure 3 shows the three-dimensional geometry of the pump jet propulsion system at the end of the AUV. The pump jet propulsion system and the AUV body are analyzed together in this analysis. Of course, in this section, we have focused on analyzing the pump jet propulsion system. The pump jet system is the rotor-stator type and has a diameter of 30 cm. The duct is of the reducing type. The length of the AUV is about 2.5 meters. In Table 1, the geometric characteristics of the pump jet propulsion are presented. The geometry of the rotor blade and stator is extracted based on the relationships of marine propellers [15].

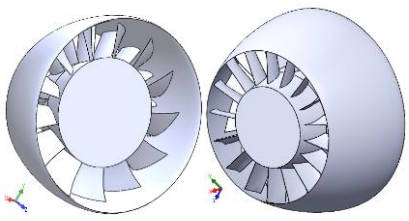

Figure.3 Geometry of designed pump jet propulsion system

Table 1. Geometric specifications of the designed pump jet

Properties	Value
Diameter [m]	0.30
Rotor blades number	15
Stator blades number	21
Duct type	decelerator
Duct inlet diameter [m]	0.30
Duct outlet diameter [m]	0.24
Duct attack angle [deg]	8
Duct Length [m]	0.28
EAR (rotor and stator)	0.8

3. Governing equations of fluid flow [16]

The governing equations of fluid flow include the equations of continuity and momentum (Navier-Stokes equations). The continuity equation for compressible fluids is expressed as follows:

$$\frac{\partial \rho}{\partial t} + \nabla.(\rho V) = 0 \qquad (1)$$

Where V is the velocity vector and ρ is the density.
The form of the Navier-Stokes equation is as follows:

$$\rho \frac{DV}{Dt} = \rho f - \nabla P + \mu \nabla^2 V \qquad (3)$$

P is the pressure, f is the volumetric force, and μ is the viscosity. The $\frac{D}{Dt}$ Operator represents a material derivative. In marine propulsion systems, the energy equation can be ignored due to the very low rate of heat transfer.

4. Grid generation and computational domain

In this section, the computational grid used in the numerical solution will be explained to simulate the flow around the body. Figure 4 schematically shows the input and output boundaries of the solution domain zone relative to the body's position.

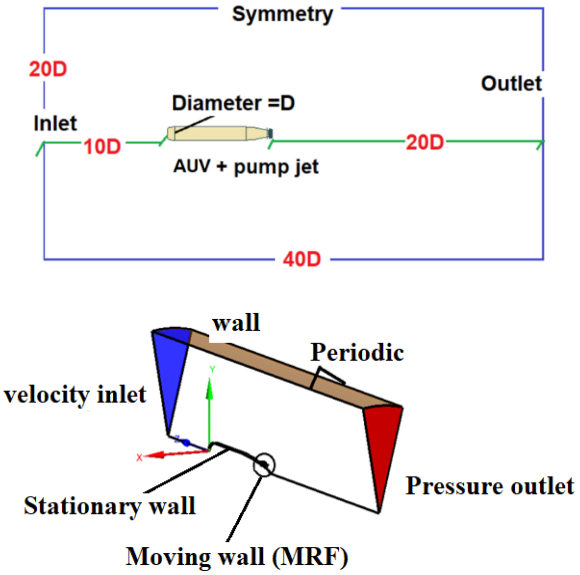

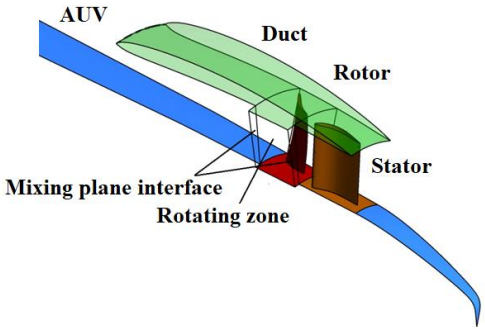

Figure.4 Schematic of the computational domain

The grid used is shown in Figure 5. Using the hybrid grid, periodic boundary conditions, and grid optimization methods have made it possible to solve this problem in 3D with less than 1.2 million cells. The produced grid is of high quality. In Figure 6, the quality of the grid based on cell skewness is shown. Figure 7 shows the grid quality based on the cell aspect ratio to solve the problem. Comparing these two Figures 6 and 7, we can see that most cells are in the excellent to acceptable range. Therefore, from the numerical solution perspective, the convergence of the solution process is expected to be desirable.

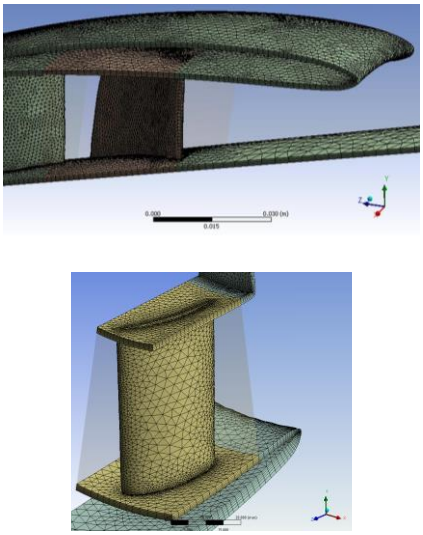

Figure.5 Grid generated on the pump jet propulsion system

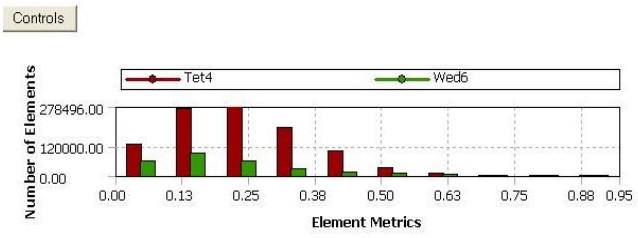

Figure.6 quality of the cells produced in terms of skewness

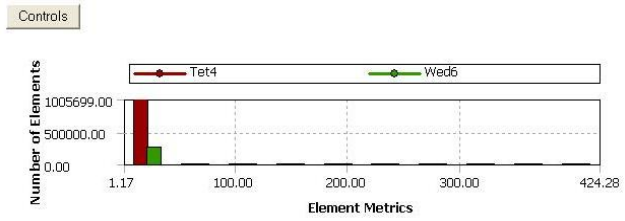

Figure.7 quality of the cells produced in terms of aspect ratio

The maximum skewness occurred in the grid is 0.94 (Figure 6), and more than 99.6% of the grid has an aspect ratio of less than 32 (Figure 7). In the existing grid, 99.99% of the total grid cells created in the cell skewness range are below 0.8, which has excellent to good quality, and in this regard, the quality of the entire grid is confirmed in terms of skewness.

The grid used in the numerical solution combines structured and unstructured networks. It can be said that except for the area close to the body, due to the modeling of viscosity effects, turbulence model considerations, and the intensity of velocity and pressure gradients, there is no need for the fine grid in other areas of the flow field. Therefore, in the production of the network, to reduce the computational cost, near the body, a structured grid and around it, an unstructured grid has produced. As can be seen, the grid in the vicinity of the object has become finer. It is required to use a denser mesh near the body to have a good resolution for capturing the velocity and the pressure fields correctly. Therefore, the dimensions of the cells are directly related to their distance from the body. In other words, the network changes from a fine grid approximately the object to a coarse grid away from the body.

5. Flow conditions

Table 2 shows the flow conditions and fluid properties. In this study, incompressible fluid is considered. The translational and rotational speeds of the rotor are constant, and the analysis is performed under steady-state conditions. Fluid properties are also assumed to be constant.

Table 2. Specifications of fluid flow solution conditions

Characteristic	Value
Fluid	Water
Density	1025 [kg/m^3]
kinematic viscosity	*1e-6* [m^2/s]
Velocity	40 [knot]
Rotational speed	2000 [RPM]
Advance ratio (J)	1 ~ 3.5

6. Solution specifications

The main purpose is to simulate the rotational motion of the rotor. The situation is such that the body (AUV + pump jet) is enclosed within a cylindrical zone. The boundaries of this zone are so far from the body that the pressure changes due to the presence of the body on the outer surfaces of the computational domain can be ignored; in other words, the body is moving in an infinite fluid.

The equations used in the solution behave like partial elliptic differential equations; therefore, the boundary conditions on all boundaries must be specified to solve. The turbulence model used to simulate the flow is the k-ε model. Thus, the equations of continuity, momentum in three directions, the kinetic energy of turbulence, and dissipation are solved together in a coupling. In the k-ε model, the standard wall function is used. Therefore, the y+ range of the first cell adjacent to the body should be between 30 and 600, although its value should preferably be close to the lower limit of this interval. This range is related to the logarithmic boundary layer in the boundary layer adjacent to the wall. The solution is performed using Fluent software. Table 3 shows the solution conditions.

Table3. Settings of fluid flow numerical solution

Value	Characteristic
Solver	Pressure based
Formulation	Implicit
Discretization Scheme	Second Order Upwind
Turbulent model	Realizable k-ε With Standard Wall function

- **DTMB4119 marine propeller benchmark**

To validate the numerical results with experimental data [17,18], the geometry of the DTMB4119 benchmark propeller has been used. Because there is no valid empirical available data regarding the pump jet. The propeller geometry and 3D modeling are shown in figure 5.

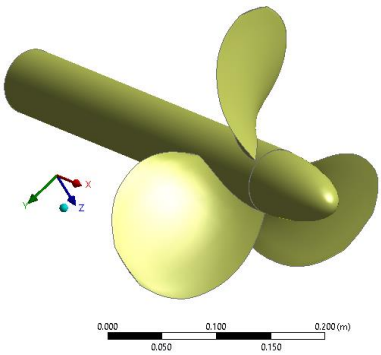

Figure.8 DTMB4119 benchmark marine propeller modeled in the present study

The incoming and rotational speeds of the propeller are 2.54 m/s and 10 rpm, respectively [18].

The computational domain for the numerical analysis is a combination of two rotating and stationary zones, cylindrical and connected by interface surfaces. The dimensions of the rotating zone are a cylinder with a diameter of 1.1D and a length of 0.65D and a fixed domain of a cylinder with a diameter of 3D and a length

of 5D. The boundary layer grid is applied on the propeller surfaces, and the unstructured grid is used far from the propeller.

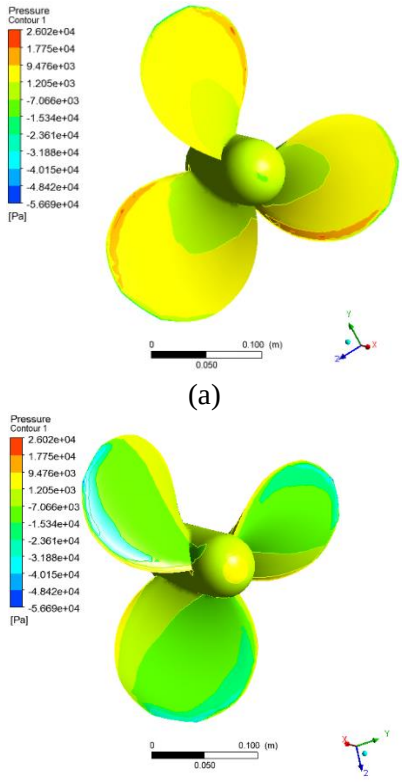

Figure.9 Contour of static pressure on DTMB4119 marine propeller: a)face side, b)backside

Grid independency

The thrust and torque coefficients have been investigated at the advance coefficient of J=0.7 to check the grid independency. The results of the last 3 modes, i.e., 2.8, 3, and 4.2 million grids, are very close. Still, the 3 million grid mode was considered to achieve the desired accuracy, and all calculations were performed in this grid number.

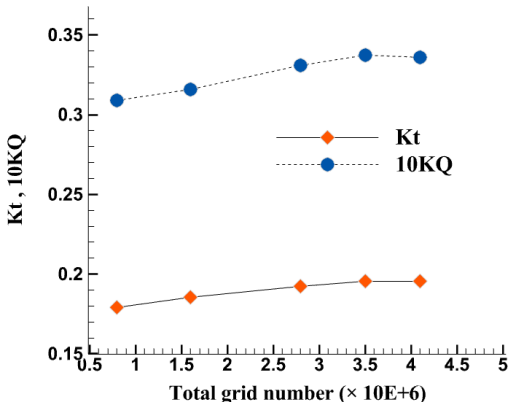

Figure.10 Grid independency on DTMB4119 benchmark propeller versus the number of elements

- **Validation of numerical result on DTMB4119**

Calculating the pressure coefficient is one of the essential parameters for estimating hydrodynamic performance. Figure 11 compares the pressure distribution on the back and face sides of the DTMB4119 propeller in the section of r/R=0.7. The present numerical results show good correlations with experimental data.

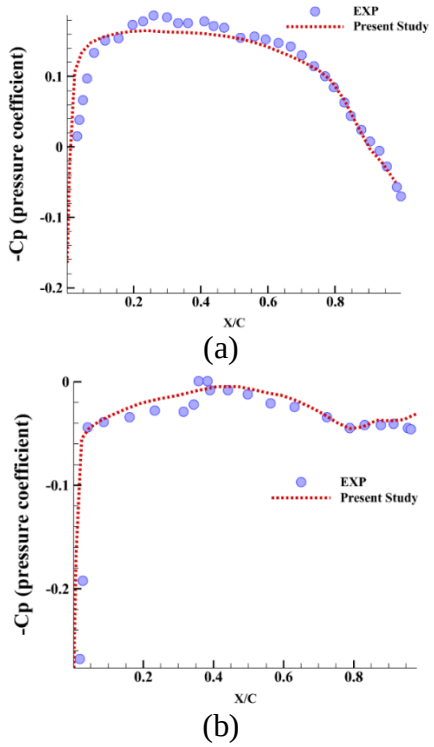

Figure.11 Numerical result of pressure coefficient on DTMB4119 propeller blade section at r/R=0.7 compared with corresponding experimental data [17]: a) backside b) face side

A comparison of the thrust and torque coefficients of the DTMB4119 propeller is shown in Figure 12. There is a good accommodation between obtained numerical data and experimental data. Generally, the error is less than 7%. It can be interpreted that in very low advanced coefficients, considering the assumption, error increases due to heavy conditions.

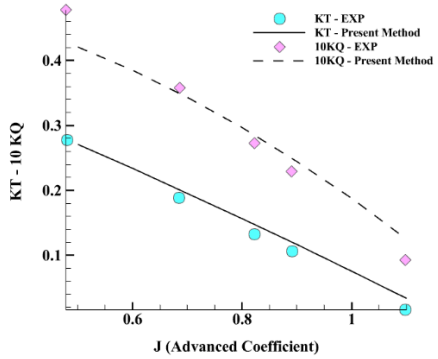

Figure.12 Numerical results of KT and 10KQ compared with corresponding experimental data[18] at various advance ratios

7. Hydrodynamic Results

Figure 13 shows the side view of the duct and stator-rotor in a semi-transparent way so that the duct section and the position of the hub and blades can be seen simultaneously.

Along the fluid flow, the duct diameter becomes smaller. Rotating the rotor and accelerating the fluid in a converging nozzle increases the fluid pressure inside the duct. The pressure on the outer surface of the duct is determined only by the pressure field of the free flow around the AUV. This pressure difference between the inside and outside of the duct creates a force that is divided into two axial and radial components. The radial component is completely neutralized because of the symmetry. Still, the axial force forms from integrating pressure and viscous generated shear stresses over the projection of the duct's surfaces. According to obtained results, the value of pressure drag force in the total drag force of the duct is dominant. Of course, the amount of viscous force is not small compared to other components, which is due to the rotor's high flow velocity in this area due to the rapid rotation of the rotor.

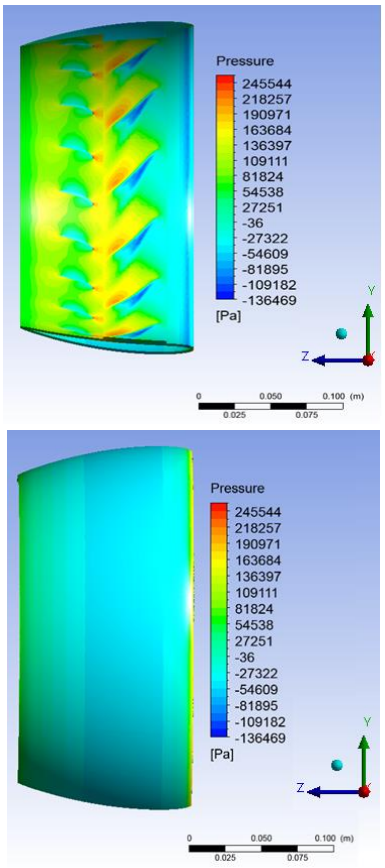

Figure.13 Contour of static pressure on the iso surface of pump jet and duct

The convergent shape of the duct causes a rapid change in the pressure field inside the duct. The pressure inside the duct is obtained from the rotation of the rotor, which the rotor does by accelerating the fluid particles. Therefore, less pressure will be applied to the rotor blades if the duct has a smooth convergence. This operation has an optimal mode. Further convergence of the duct creates more pressure on the rotor blades, which increases the thrust on rotor blades (which is a good effect) and increases the drag force generated by the duct. If the convergence is smoother, the pressure generated on the rotor will be reduced, resulting in less thrust on the blades and a negative effect, but it will also reduce drag on the duct. Therefore, there will be an optimal state during which these components generate the maximum total thrust. The figure below shows the pressure contour from the front and back of the rotor blades (Figure. 14).

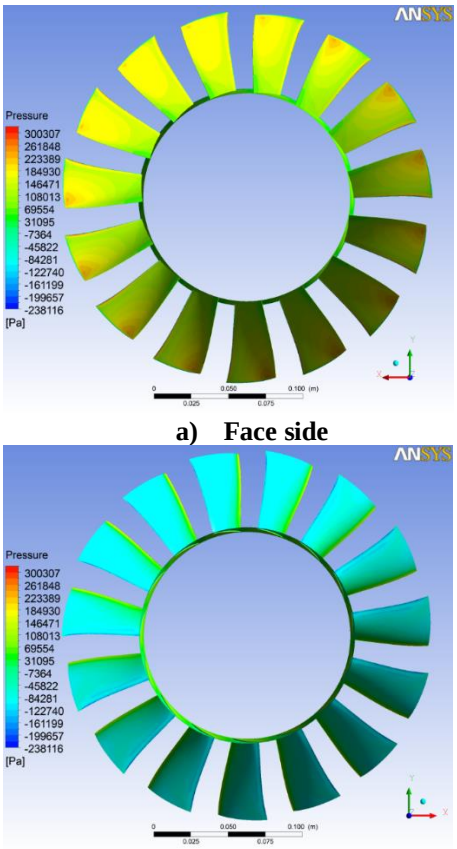

a) Face side

b) Back side

Figure.14 Contour of static pressure on the rotor face and back sides

The rotor hub generates thrust due to the slope of the geometry and the pressure field resulting from the rotation of the rotor. Due to the flow direction in this part, viscous force is still the cause of drag production, but the share of compressive force in this part is also dominant, which is the reason for thrust force. This is well illustrated in Figure 15.

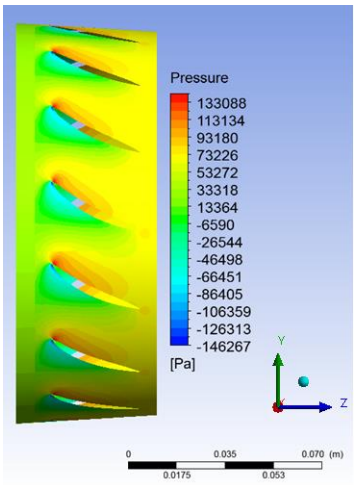

Figure.15 Contour of static pressure on the rotor hub

The stator blades are designed to correct the outlet angle of the flow from the rotor at the exit from the duct. It is also predicted that thrust will be generated at the end of the stator blades.

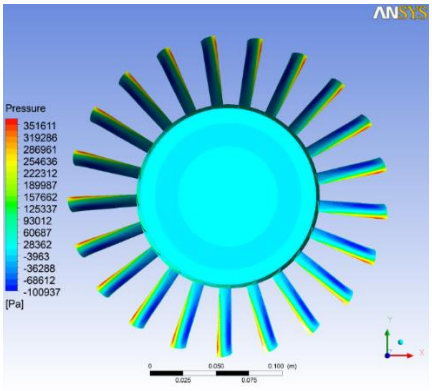

a) Face side

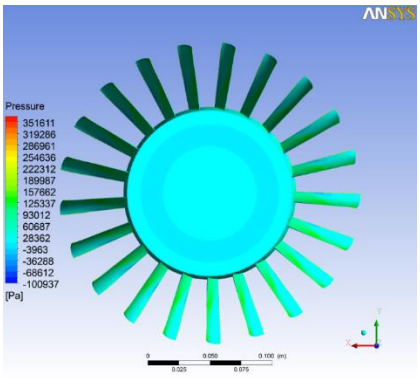

b) Back side

Figure.16 Contour of static pressure on the stator face and back sides

In stator blades, the pressure field is formed by deviating the flow direction so that the pressure on the concave side of the blades is more than its convex side. Like the action in turbine blades, the fluid kinetic energy is converted into a pressure field and causes a force to be applied to the blade.

The viscous force applied from the fluid to the blades creates a resistance force, while the pressure field in this area gives thrust force. Figure 16 shows the front and back sides' pressure contours on the stator blades. A high-pressure area is formed at the blade's edge of the convex surface. The reason for this high-pressure area, which is undesirable, is the high twist of the blade tip so that the flow coming out of the rotor blades hits the back edge of the stator blades. This problem can be solved by reducing this angle in the stator blades. The stator hub has also produced a thrust due to the increase in fluid pressure in the direction of flow through the duct. (Figure 17)

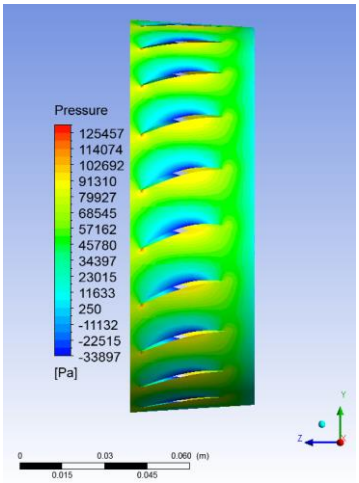

Figure.17 Contour of static pressure on the stator hub

7.1 Pump jet hydrodynamic performance

In this section, the performance curve of the pump jet propulsion system, including thrust coefficient, torque coefficient, and total hydrodynamic efficiency, has been extracted using the obtained numerical results.

The thrust and torque coefficients of different components are presented separately to better understand the performance of each component of the propulsion system. Figure 18 shows the thrust coefficient versus advance ratio. According to obtained results, the rotor and stator thrust coefficient changes in the advance coefficient are much less compared to conventional propulsion systems. But as can be seen, due to the lack of proper design of the duct profile, the drag force of the duct has neutralized a significant part of the thrust produced by the rotor and stator, especially at high advance coefficients. This subject shows that the design of the duct profile plays an important role in the performance of the pump jet propulsion system.

In addition, the results for the open water condition in 4 states J=2.3, 2.5, 2.7, 2.9 are presented in this figure. The results show that the thrust coefficient of the rotor and stator have changed relatively little compared to the case with the body, but the coefficients obtained for the duct with and without the body have changed by about 15% to 20%.

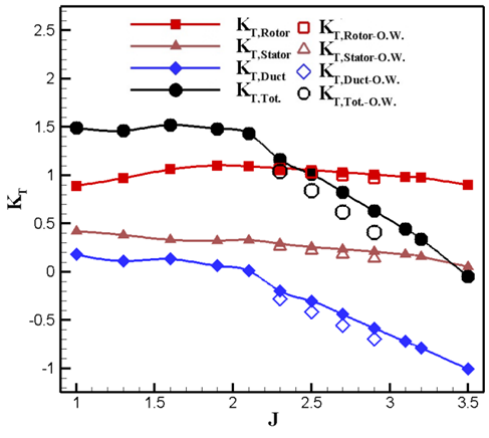

Figure.18 Comparison of the thrust coefficients of different components in open water and behind the AUV body

Figure 19 presents the results of the rotor and stator torque coefficient as well as the total torque coefficient. The sign of the rotor and stator torque coefficients must be different. For better comparison, only the size of the torque values is shown in this figure. As can be seen, the obtained torque coefficient is relatively constant in all cases and especially in higher advance ratios.
Also, figure 19 shows the torque coefficient of the free water state. A similar trend is observed for open water and body conditions changes. Since the total thrust coefficient of the free water mode is higher than that of the body mode and the rotor roll torque is almost the same in both modes, the overall efficiency of the free water mode is higher. According to the figure, the efficiency of the pump-jet propulsion system in operating mode is in the range of $0.30 \leq \eta \leq 0.80$, and its maximum efficiency is about 20% higher than that of conventional propeller propulsion systems.

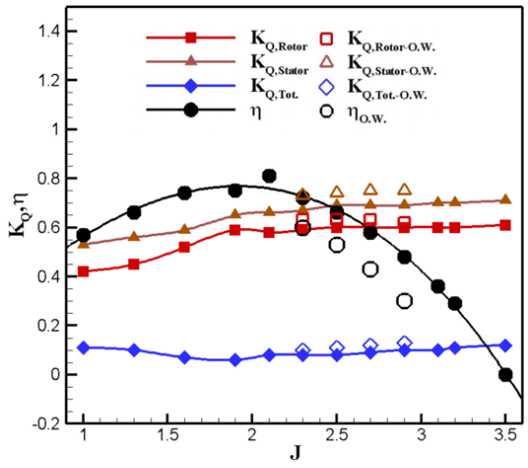

Figure.19 Comparison of the torque coefficients of different components in open water and behind the AUV body

8. Structural analysis and calculation of natural vibrations

This section performs static analysis of the pump jet propulsion system and calculation of natural frequencies.

8.1. Modeling and grid generation of stator blades

Due to the importance of networking in the finite element method, modeling parts has been done in Abacus software to create cubic elements and avoid the use of pyramidal elements. The element type, C3D20R, has been selected as a second-order element with reduced integration points. The number of elements in the thickness is 5, which makes the results correct even with linear elements. (Figure 20)

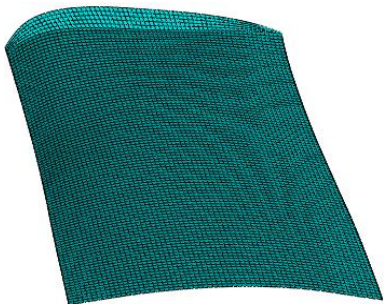

Figure.20 grid generated on the stator blade

The boundary conditions for the stator have some uncertainty. Therefore, the analysis was based on two models. In the first model, only the stator was modeled, and the upper part of the stator was closed. The parts connected to the stator were also modeled in the second model. Finally, only the duct was closed at the locations shown in Figures 21 and 22. The pressure on the blades was applied point by point based on the results of the CFD analysis. Therefore, no simplifying assumption has been applied in this study. The material of the stator is aluminum with a Young modulus of 70 GPa.

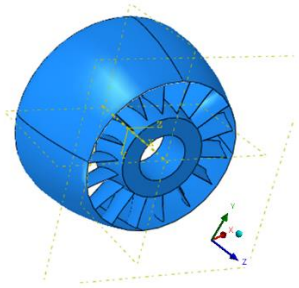

Figure.21 Stator model and its connected parts

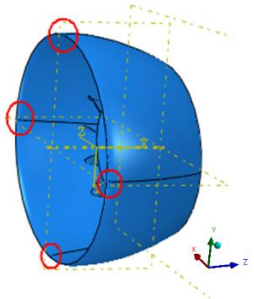

Figure.22 Closed locations in stator analysis

8.2. Grid independence study

Grid convergence determines how many elements are required in a model to ensure that the results of an analysis are not affected by changing the size of the computational elements. Grid convergence is an important consideration in ABAQUS software. In this section, the considered parameter to check the grid independence is the maximum value of Von Mises stress on the pump jet propulsion system. Figure 23 shows maximum Von Mises stress variations based on the number of computational elements for a one-rotor blade. According to the figure, after 60,000 elements, there is no change in the value of the results.
Figure 24 shows the maximum Von Mises stress variations versus the changes in the number of elements on the duct, hub, and stator blades.
The number of suitable elements to satisfy the grid independence condition is about 3.9 million.
Therefore, the total number of elements to satisfy the grid independency of the pump jet propulsion system is 4.8 million elements.

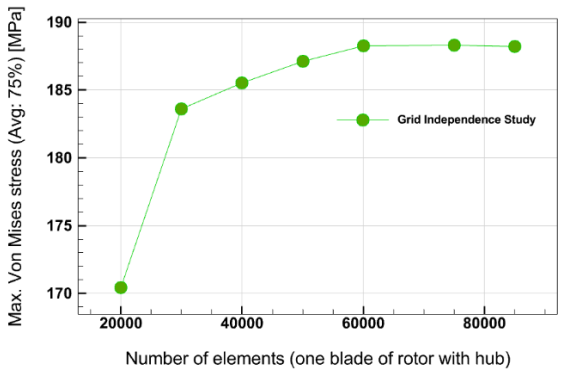

Figure.23 Grid independency of max Von Mises stress on stator separately versus the number of elements

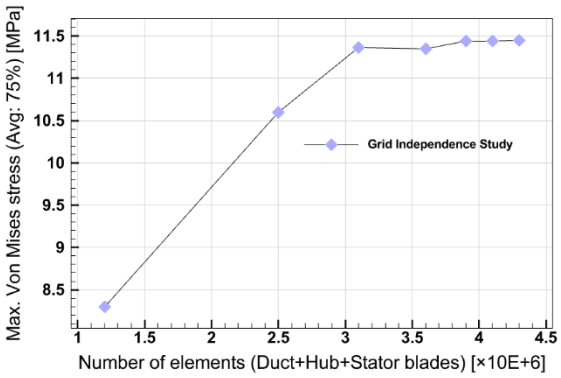

Figure.24 Grid independency of max Von Mises stress on duct+Hub+stator versus the number of elements

8.3. Calculation of the stator blade tension

The stress obtained in the stator while the stator is analyzed separately is shown in Figure 25. Due to the stress concentration, this value is more than the real value. In practice, this stress concentration will disappear due to the presence of fillets in the body. Therefore, this stress cannot be a design criterion.

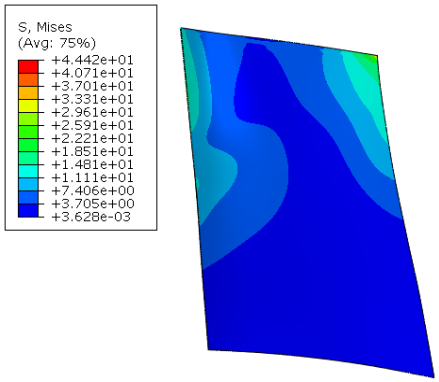

Figure.25 The amount of tension in the stator separately

By removing the stress of the corner elements, the appropriate stress value for the design will be obtained in Figure 26, with a maximum value of 27.6 MPa.

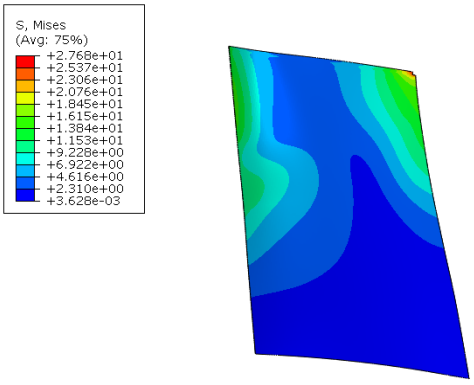

Figure.26 The amount of stress in a separate stator by removing the amount of stress in the corner elements

If the whole pump jet propulsion body is analyzed, the maximum amount of stress will be 11.5 MPa, which is much less than the previous value. (Figure 27)

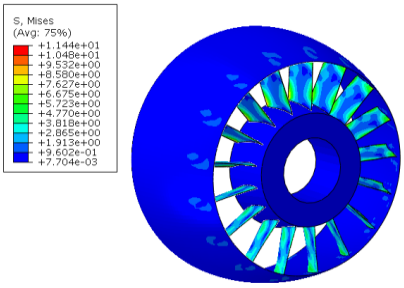

Figure.27 The amount of tension on the hub, duct, and stator

8.4. Numerical analysis of the natural frequency of the stator blade

The first, second, and third natural frequencies of the stator are shown in Figures 26 ~28. Given that the rotor rotational speed is about 2000 rpm, given the presence of 13 blades in the rotor, the excitation frequency will be 433 rpm. The stator blades will intensify at the first frequency, given that the first natural frequency is 428 and the excitation frequency is about 433 rpm. Therefore, the stator blade structures must be strengthened due to the low natural frequency.

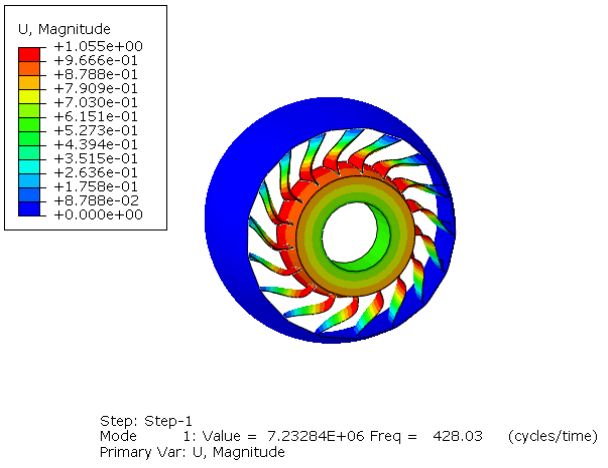

Figure.26 The first natural frequency of the stator

The second and third frequencies are related to the duct strength, which is lower than normal due to the point boundary conditions. Therefore, if the duct connections are suitable, there will be no particular problem.

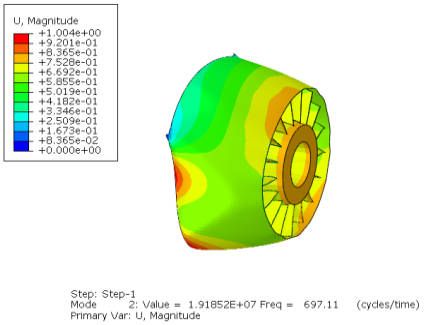

Figure.27 The second natural frequency of the stator

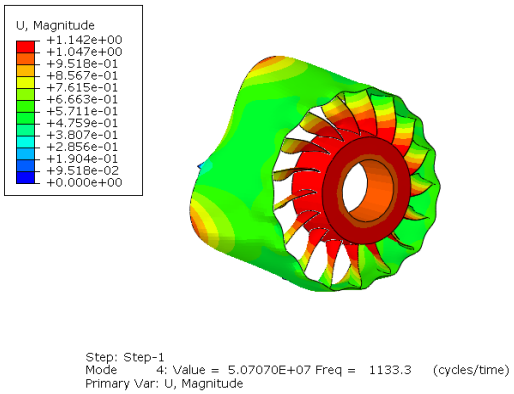

Figure.28 The third natural frequency of the stator

8.5. Calculation of the rotor blade tension

Rotor modeling is done similarly to the stator and is shown in Figure 29. The element type, C3D20R, has been selected as a second-order element with reduced reduction points. The number of elements is 5 in the thickness direction, which has led to the accuracy of the results even with linear elements.

The rotor boundary conditions are applied at the bottom of the rotor, and the rotor is completely closed in this part. The pressure on the rotor obtained from the CFD results is applied point by point. Due to the rotational motion of the rotor blade, centrifugal force is also applied in this analysis. The rotational speed value is 2000 rpm. The rotor blade is aluminum with a Young modulus of 70 GPa.

Figure.29 Grid generated on the rotor blades

8.6. Rotor blade stress analysis

The amount of stress obtained in the rotor in the case of centrifugal force removal is shown in Figure 30. This stress is higher than the actual values due to the stress concentration and neglect of the fillets.

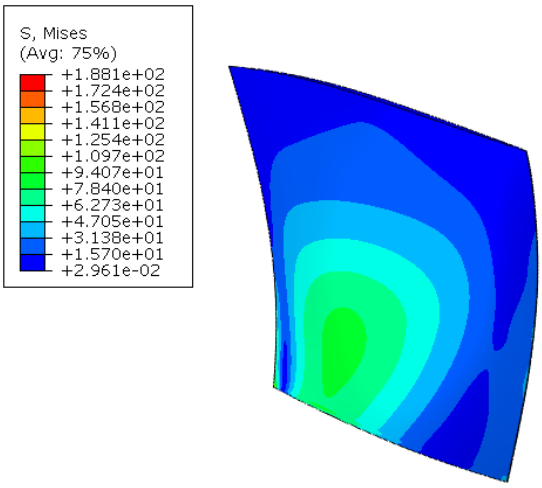

Figure.30 Tension in the rotor blade without centrifugal force

Figure 31 shows the number of stresses by removing the corner elements. Accordingly, the amount of stress in the rotor blade is 115 MPa.

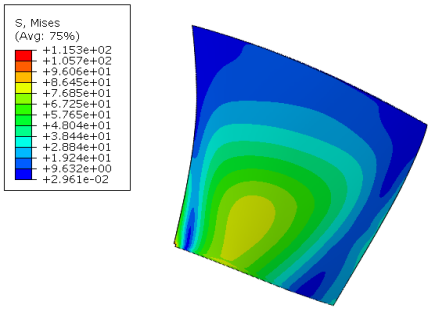

Figure.31 Tension in the rotor blade without centrifugal force by removing the corner elements

If the centrifugal forces are considered, the rotor blade's stress will change very little. These stresses are shown in Figure 32.

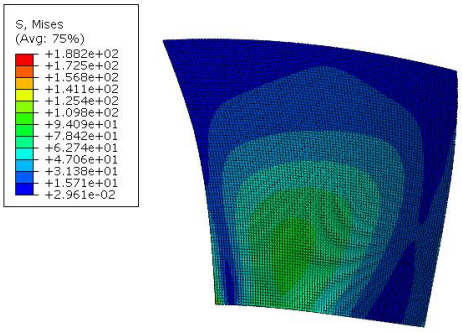

Figure. 32 Tension in the rotor blade, taking into account the centrifugal force

8.7. Rotor natural frequency analysis

The first, second, and third natural frequencies of the rotor blades are shown in Figure 33, Figure 34, and Figure 35. The natural frequency of the rotor blade is more than 800 rpm. According to the rotor speed of 2000 rpm, the excitation frequency is 433 rpm. Therefore, the rotor will not have a problem in terms of vibrations.

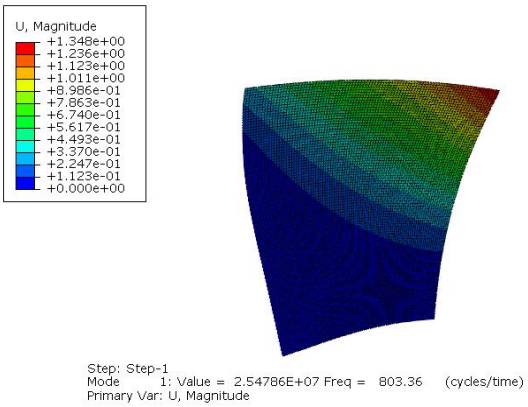

Figure.33 The first frequency of the rotor blade

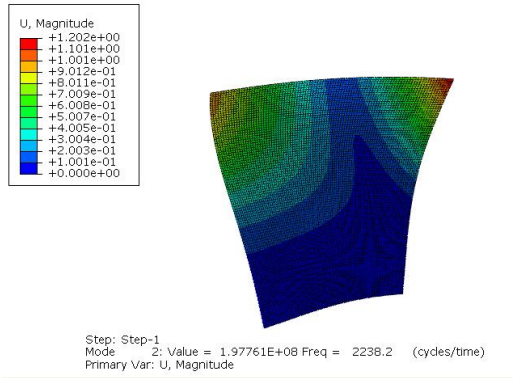

Figure.34 The second frequency of the rotor blade

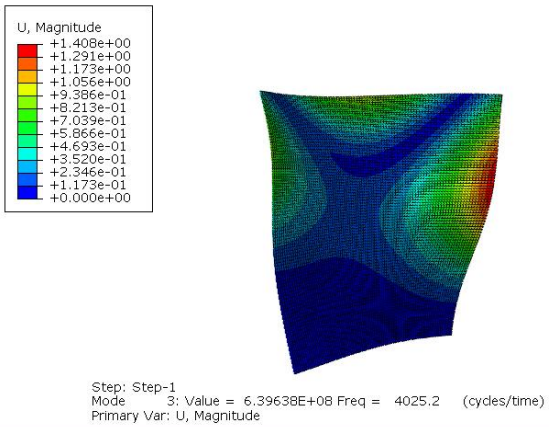

Figure.35 The third frequency of the rotor blade

9. Conclusions

In this paper, the numerical study of the pump jet propulsion system from the perspective of hydrodynamic, structures and vibrations was studied. The propulsion system of the pump jet is of the rotor-stator type, mostly used in underwater projectiles and torpedoes. Some of the most important results are summarized below:

- The obtained force and moment results show that the stator blades neutralize a maximum of 85% of the torque generated by the rotor blades. Therefore, to neutralize the roll moment caused by the rotor, it is necessary to be given an initial angle to the body control surfaces or use lifting surfaces in the body aft.
- In producing the geometry of the jet pump propulsion system, the rotor and stator blades are located at the end of the duct, and this can reduce the diameter of the pump jet system. Small propulsion system diameter reduces the amount of ventilation when moving near the free surface.
- The pressure in the stator blade field is formed by deviating the flow direction so that the pressure on the concave side of the blades is more than its convex side. Like the action in turbine blades, the fluid kinetic inertia is converted into a pressure field and causes a force to be applied to the blade.
- The rotor blade withstands relatively high stresses, which limits the type of alloy used. Considering the reliability coefficient 2, the type of rotor material should be aluminum with a yield stress of more than 220 MPa. The rotor blade will not have a problem in terms of natural frequency.

10. References

1- Ch. Suryanarayana, B. Satyanarayana, K. Ramji, (2001), *Performance evaluation of an underwater body and pump jet by model testing in cavitation tunnel*, International Journal of Naval Architecture and Ocean Engineering, Volume 2, Issue 2, Pages 57-67.

2- Stefan Ivanell, (2001), *Hydrodynamic simulation of a torpedo with pump jet propulsion system*, Master's thesis, Royal Institute of Technology, Stockholm, Sweden.

3- D. Zhang, W. Shi, B. Chen and X. Guan, (2010), Unsteady *flow analysis and experimental investigation of axial-flow pump*, Journal of Hydrodynamics, vol. 22, no. 1, pp. 35-43.

4- S. Bozorgi, M.S. Seif and M. Khaiatian, (2013), *Determining the performance characteristics of the pump jet system numerically*, 15th Marine Industries Conference, Iran, Kish Island.

5- Lü, Xiao-Jun & Zhou, Qi-Dou & Fang, Bin, (2014), *Hydrodynamic performance of distributed pump-jet propulsion system for underwater vehicle*, Journal of Hydrodynamics, Ser. B. 26. 523–530.

6- Pan, Guang & Lu, Lin & Sahoo, Prasanta, (2015), *Numerical simulation of unsteady cavitating flows of pumpjet propulsor*, Ships and Offshore Structures. 11. 1-11.

7- Yari, E., & Ghassemi, H, (2016), *Free and forced vibrations of a shaft and propeller using the couple of finite volume method, boundary element method and finite element method*, Journal of computational methods in engineering (ESTEGHLAL), 34(2), 13-36. (In Persian)

8- Lu, Lin & Pan, Guang & Wei, Jing & Pan, Yipeng, (2016), *Numerical simulation of tip clearance impact on a pumpjet propulsor*, International Journal of Naval Architecture and Ocean Engineering. 8.

9- Lu, Lin & Pan, Guang & Sahoo, Prasanta, (2016), *CFD prediction and simulation of a pumpjet propulsor*, International Journal of Naval Architecture and Ocean Engineering. 8.

10- Qin, Denghui & Pan, Guang & Qiaogao, Huang & Zhang, Zhengdong & Ke, Jiujiu, (2017), *Numerical Investigation of Different Tip Clearances Effect on the Hydrodynamic Performance of Pumpjet Propulsor*, International Journal of Computational Methods. 15. 1850037.

11- M Motallebi-Nejad, M Bakhtiari, H Ghassemi, M Fadavie, (2017), *Numerical analysis of ducted propeller and pump jet propulsion system using periodic computational domain*, Journal of Marine Science and Technology 22 (3), 559-573.

12- Qin, Denghui & Qiaogao, Huang & Shi, Yuejun & Pan, Guang & Shi, Yao & Dong, Xinguo, (2021), *Comparison of hydrodynamic performance and wake vortices of two typical types of pumpjet propulsor*. Ocean Engineering. 224. 108700.

13- Hu Jian, Weng Kaiqiang, Wang Chao, Gu Lang, Guo Chunyu, (2021), *Prediction of hydrodynamic performance of pump jet propulsor considering the effect of gap flow model*, Ocean Engineering, Volume 233.

14- Zhiwei Su, Shuaikang Shi, Xiuchang Huang, Zhiqiang Rao, Hongxing Hua, (2021), *Vibro-acoustic characteristics of a coupled pump-jet – Shafting system – SUBOFF model under distributed unsteady hydrodynamics by a pump-jet*, Ocean Engineering, Volume 235.

15- John Carlton, (2018), *Marine propellers and propulsion*, 4th Edition, Butterworth-Heinemann publisher.

16- Frans T.M. Nieuwstadt, Jerry Westerweel, Bendiks J. Boersma, (2016), *Turbulence: Introduction to Theory and Applications of Turbulent Flows*, 1st ed. Birkhauser Verlag AG publisher.

17- Report of the propulsor Committee, (1992), *Workshop Organized by 20th ITTC Propulsor*, 23 August, Seoul Korea.

18- K. Boumediene, S. E. Belhenniche, (2016), *Numerical analysis of the turbulent flow around DTMB 4119 marine propeller*, International Journal of Marine and Environmental Sciences, Vol:10, No:2.